ICARUS 112, 130–146 (1994)

Gravity over Coronae and Chasmata on Venus

GERALD SCHUBERT AND WILLIAM B. MOORE

Department of Earth and Space Sciences, Institute of Geophysics and Planetary Physics, University of California, Los Angeles, California 90024-1567
E-mail: gschubert@mgnvax.ess.ucla.edu

AND

DAVID T. SANDWELL

Institute of Geophysics and Planetary Physics, Scripps Institute of Oceanography, La Jolla, California 92093

Received March 16, 1994; revised August 19, 1994

The global spherical harmonic model of Venus' gravity field MGNP60FSAAP, with horizontal resolution of about 600 km, shows that most coronae have little or no signature in the gravity field. Nevertheless, some coronae and some segments of chasmata are associated with distinct positive gravity anomalies. No corona has been found to have a negative gravity anomaly. The spatial coincidence of the gravity highs over four closely spaced 300- to 400-km-diameter coronae in Eastern Eistla Regio with the structures themselves is remarkable and argues for a near-surface or lithospheric origin of the gravity signals over such relatively small features. Apparent depths of compensation (ADCs) of the prominent gravity anomalies at Artemis, Latona, and Heng-o Coronae are about 150 to 200 km. The geoid/topography ratios (GTRs) at Artemis, Latona, and Heng-o Coronae lie in the range 32 to 35 m km^{-1}. The large ADCs and GTRs of Artemis, Latona, and Heng-o Coronae are consistent with topographically related gravity and a thick Venus lithosphere or shallowly compensated topography and deep positive mass anomalies due to subduction or underthrusting at these coronae. At arcuate segments of Hecate and Parga Chasmata ADCs are about 125 to 150 km, while those at Fatua Corona, four coronae in Eastern Eistla Regio, and an arcuate segment of Western Parga Chasma are about 75 km. The GTRs at Fatua Corona, the four coronae in eastern Eistla Regio, and the arcuate segments of Hecate, Parga, and Western Parga Chasmata are about 12 to 21 m km^{-1}. The ADCs and GTRs of these coronae and arcuate chasmata segments are generally too large to reflect compensation by crustal thickness variations. Instead, they suggest compensation by thermally induced thickness variations in a moderately thick ($\approx$100 km) lithosphere. Alternatively, the gravity signals at these sites could originate from deep positive mass anomalies due to subduction or underthrusting. Weighted linear least squares fits to GTR vs h (long-wavelength topography) data from Heng-o and Fatua Coronae, the four coronae in eastern Eistla Regio, and the arcuate segments of Hecate, Parga, and western Parga Chasmata are consistent with compensation by thermally induced thickness variations of a dense lithosphere above a less dense mantle; the fits imply an average lithosphere thickness of about 180 km and an excess lithospheric density of about 0.5 to 0.7%. Gravity anomalies at the arcuate segments of Dali and Diana Chasmata that form Latona Corona, at Artemis Chasma, and other arcuate segments of Parga and Hecate Chasmata occur on the concave sides of the arcs. By analogy with gravity anomalies of similar horizontal scale (600 km–several thousand kilometers) on the concave sides of terrestrial subduction zone arcs, which are due in large part to subducted lithosphere, it is inferred that the gravity anomalies on Venus are consistent with retrograde subduction at Artemis Chasma, along the northern and southern margins of Latona Corona, and elsewhere along Parga and Hecate Chasmata.

1. INTRODUCTION

Coronae are geologic structures unique to Venus that are characterized by quasi-circular rings of tectonic deformation. Chasmata are very long, narrow and deep troughs or chasms that extend for thousands of kilometers away from the major volcanic rises on Venus. Arcuate segments of asymmetric chasmata comprise the defining tectonic structures of Artemis and Latona Coronae. The topographic, morphologic, and geologic characteristics of coronae and chasmata have been extensively described (Stofan and Head 1990, Head *et al.* 1991, Solomon *et al.* 1991, Stofan *et al.* 1992, Squyres *et al.* 1992). However, only recently, with the acquisition of higher resolution and more complete gravity data by the Magellan spacecraft (Konopliv *et al.* 1993, Konopliv and Sjogren 1994) has it become feasible to detect the gravity signals associated with coronae and chasmata. The purpose of the present paper is to describe and interpret these gravity fields in terms of the processes that may be responsible for the formation of coronae and chasmata. In particular, we will assess whether the gravity fields over Artemis and Latona Coronae and over some arcuate segments of chasmata are consistent with possible subduction or underthrusting at these sites (Sandwell and Schubert 1992a, b, McKenzie *et al.* 1992).

0019-1035/94 $6.00

2. OBSERVATIONS

Our analysis is based on the spherical harmonic representation of the gravity field of Venus deduced from orbital tracking of both the Pioneer Venus and Magellan spacecraft (Konopliv *et al.* 1993, Konopliv and Sjogren 1994). We use version MGNP60FSAAP of the spherical harmonic gravity field, constrained locally by Kaula's rule (Kaula 1966).

The gravity signals over features considered in this paper (Artemis, Latona, Fatua, and Heng-o Coronae, a group of four coronae in eastern Eistla Regio, and segments of Hecate, Parga, and western Parga Chasmata) are shown in Figs. 1–4; gravity and other characteristics of these structures are summarized in Table I. Each of the features is discussed below.

2.1. Artemis Corona

Artemis Corona is defined by Artemis Chasma, a very deep (4–6 km) asymmetric trench that forms $\approx\frac{3}{4}$ of a circle about 2600 km in diameter. The topography (from gridded Magellan topography data; Ford and Pettengill 1992) (Fig. 1A) of the interior rises sharply from this trench forming a rim that encircles a broad plateau some 2 km above the plains that border it to the south (Table I). Another chasma system running northeast–southwest through the interior of the corona intersects Artemis Chasma in the northeast. Just to the northwest of this intersection, Artemis Chasma merges with Diana Chasma to form the border between Artemis and the tessera region Thetis Regio. The interior of Artemis Corona can be subdivided into four sections based on topographic and SAR data (Figs. 1 and 5). Most of the interior is taken up by the broad plateau (NP and SP) referred to above which is characterized by relatively smooth topography and is bounded by Artemis Chasma on the east and south and by a northeast–southwest-trending belt of deformation (chasma system, NB) on the west. This plateau may be further subdivided into a northern section (NP) composed of smooth plains-like flows with some small volcanic features, and a southern section (SP) which shows more significant tectonism and somewhat rougher topography. The border between these regions is marked by a northwest–southeast-trending belt of deformation that is made up of features that strike primarily perpendicular but also parallel to the belt. The deformed belt that borders the plateau to the west is also divided into two sections, a northern region (NB) of primarily northeast–southwest troughs and generally depressed topography, and a southern deformed block (SB), completely surrounded by a trench which intersects Artemis Chasma on the south. At this intersection tectonic structures within Artemis Chasma are more complex than elsewhere in the chasma and rim elevations are very high.

TABLE I

Summary of Gravity and Topography Data over Coronae and Chasmata

Name	Type, location	Size (km)	Peak gravity (mgal) (MGNP60FSAAP)	Peak[a] topography ($\lambda \geq 600$ km) (m)	Regional[b] mean gravity (mgal)	Regional[b] mean topography (m)	Best Fit App. depth comp. (km)	Gravity/ topography ratio (GRTR) (mgal/m)	Geoid/ topography ratio (GTR) (m/km)	Comments
Artemis	Corona (chasmata) 35S 135E	2600	42	1970	7.1	1350	200	0.056 ± 0.008	35 ± 5	The largest feature studied. The peak gravity anomaly is not centered over the corona but lies over the southeastern portion.
Latona	Corona (chasmata) 20S 170E	800	49	2440	6.9	1450	150	0.043 ± 0.007	32 ± 5	Very strong correlation of both short wavelength gravity and long wavelength geoid with topography.
Eastern Eistla Regio	Corona (4 nr. rise) 15N 45E	300–400	45	2130	6.7	826	75	0.035 ± 0.007	12 ± 2	There is very good correlation of peak gravity anomalies with each of the four coronae and with several volcanoes in the region.
Parga	Corona (chasmata) 15S 245E	500	38	1350	2.6	756	125	0.059 ± 0.017	20 ± 6	There is a gravity high associated with only one of a pair of the uplifted flanks of the chasma.
Western Parga	Corona (chasmata) 7S 222E	400	49	2280	3.0	1270	75	0.048 ± 0.014	13 ± 4	The gravity peak is associated with only one of two uplifted chasma flanks, the one forming part of the border of the corona.
Hecate	Corona (chasmata) 15N 245E	525	38	1030	−7.0	474	150	0.047 ± 0.013	15 ± 3	A gravity peak is present only over the corona, although equally high topography occurs nearby.
Heng-o	Corona (plains) 2S 355E	1060	20	722	−4.8	340	150	0.076 ± 0.017	35 ± 8	Gravity and topography peaks are associated with the southern outer rise. The GTR and GRTR are poorly constrained.
Fatua	Corona (plains) 17S 17E	310	22	880	2.4	384	75	0.064 ± 0.023	21 ± 8	The gravity peaks seem associated with portions of the outer rise but do not correlate very well with the topography, leading to a poorly constrained GRTR.

[a] Peak topography determined from 3° averaged topography.

[b] Regional mean gravity (topography) is determined from 3° averaged data for the region used to determine the GTR and GRTR.

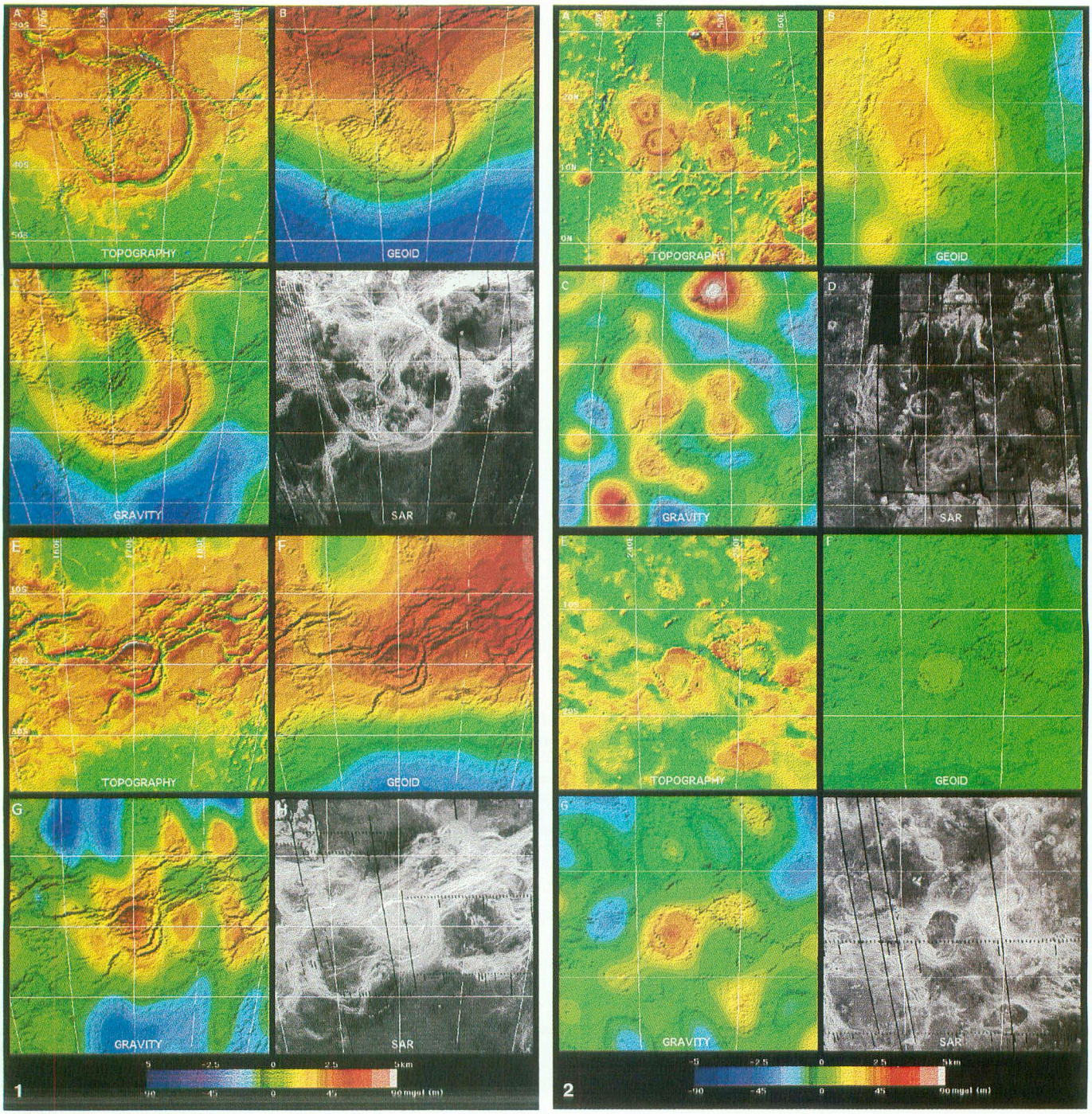

FIG 1. (Top) Artemis Corona. (A) Topography from gridded Magellan altimetry referenced to a mean planetary radius of 6051 km (B) geoid height from MGNP60FSAAP, 60th degree and order global spherical harmonic model (Konopliv *et al.* 1994), displayed over shaded relief map. (C) Gravity anomaly from MGNP60FSAAP gravity model displayed over shaded relief. (D) Magellan SAR composite. The images are centered at 35°S, 135°E and latitude and longitude lines are plotted at 10° intervals (105.6 km per degree of latitude). (Bottom) Latona Corona and Dali–Diana Chasmata region. (E) Topography, (F) geoid height, (G) gravity anomaly, (H) Magellan SAR composite. The images are centered at 20°S, 171°E. Color scales for topography (km), gravity (mgal), and geoid height (m) are given.

FIG. 2. (Top) A region of eastern Eistla Regio containing four coronae. (A) Topography, (B) geoid height, (C) gravity anomaly, (D) Magellan SAR composite. The images are centered at 15°N, 44°E. (Bottom) An area of Parga Chasma. (E) Topography, (F) geoid height, (G) gravity anomaly, (H) Magellan SAR composite. The images are centered at 15°S, 245°E. Presentation is similar to that of Fig. 1.

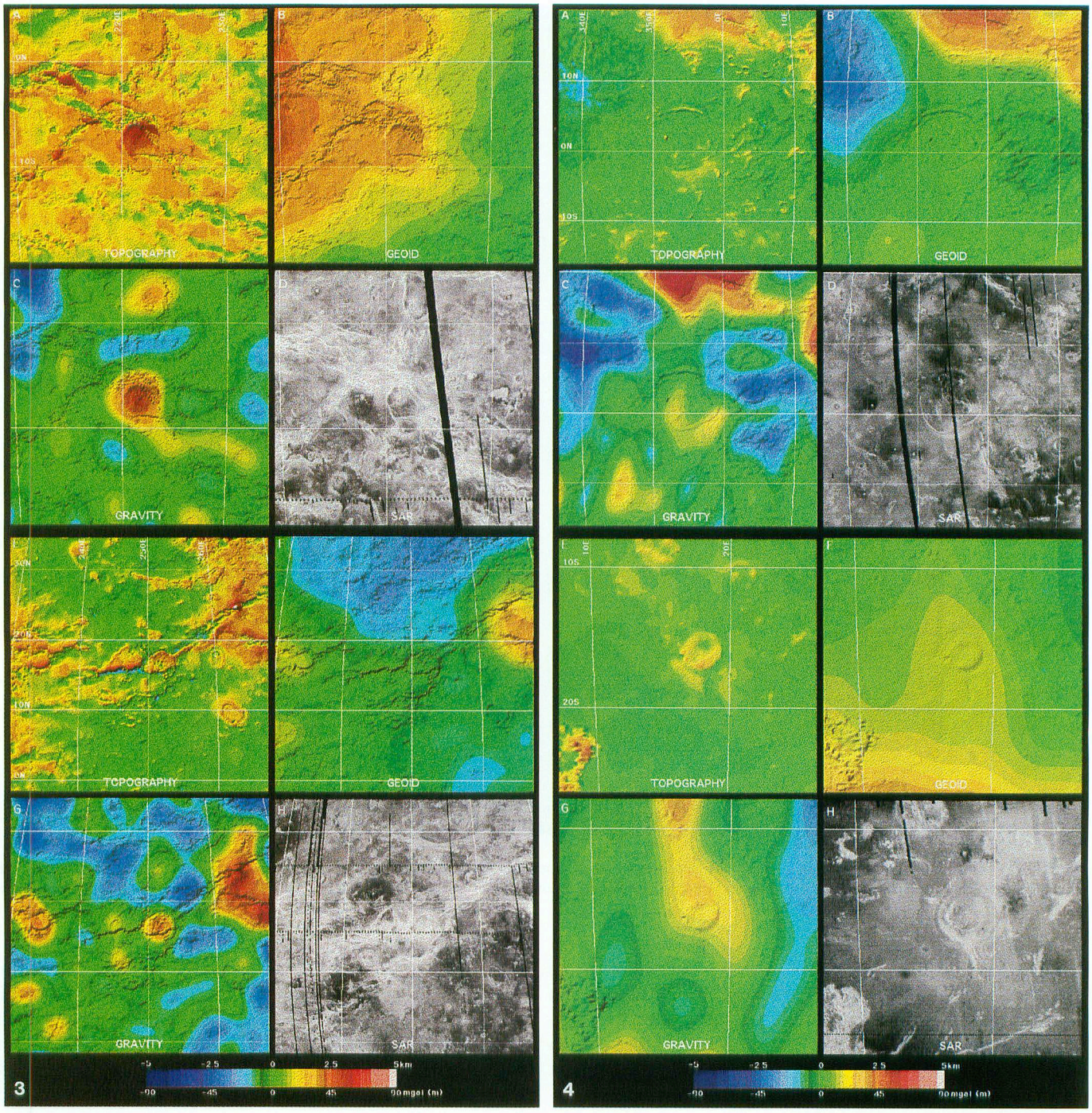

FIG. 3. (Top) A region of western Parga Chasma. (A) Topography, (B) geoid height, (C) gravity anomaly, (D) Magellan SAR composite. The images are centered at 7°S, 222°E. (Bottom) An area of Hecate Chasma. (E) Topography, (F) geoid height, (G) gravity anomaly, (H) Magellan SAR composite. The images are centered at 16°N, 249°E. Presentation is similar to that of Fig. 1.

FIG. 4. (Top) A region including Heng-o Corona. (A) Topography, (B) geoid height, (C) gravity anomaly, (D) Magellan SAR composite. The images are centered at 2°N, 355°E. (Bottom) A region containing Fatua Corona. (E) Topography, (F) geoid height, (G) gravity anomaly, (H) Magellan SAR composite. The images are centered at 17°S, 17°E. Presentation is similar to that of Fig. 1.

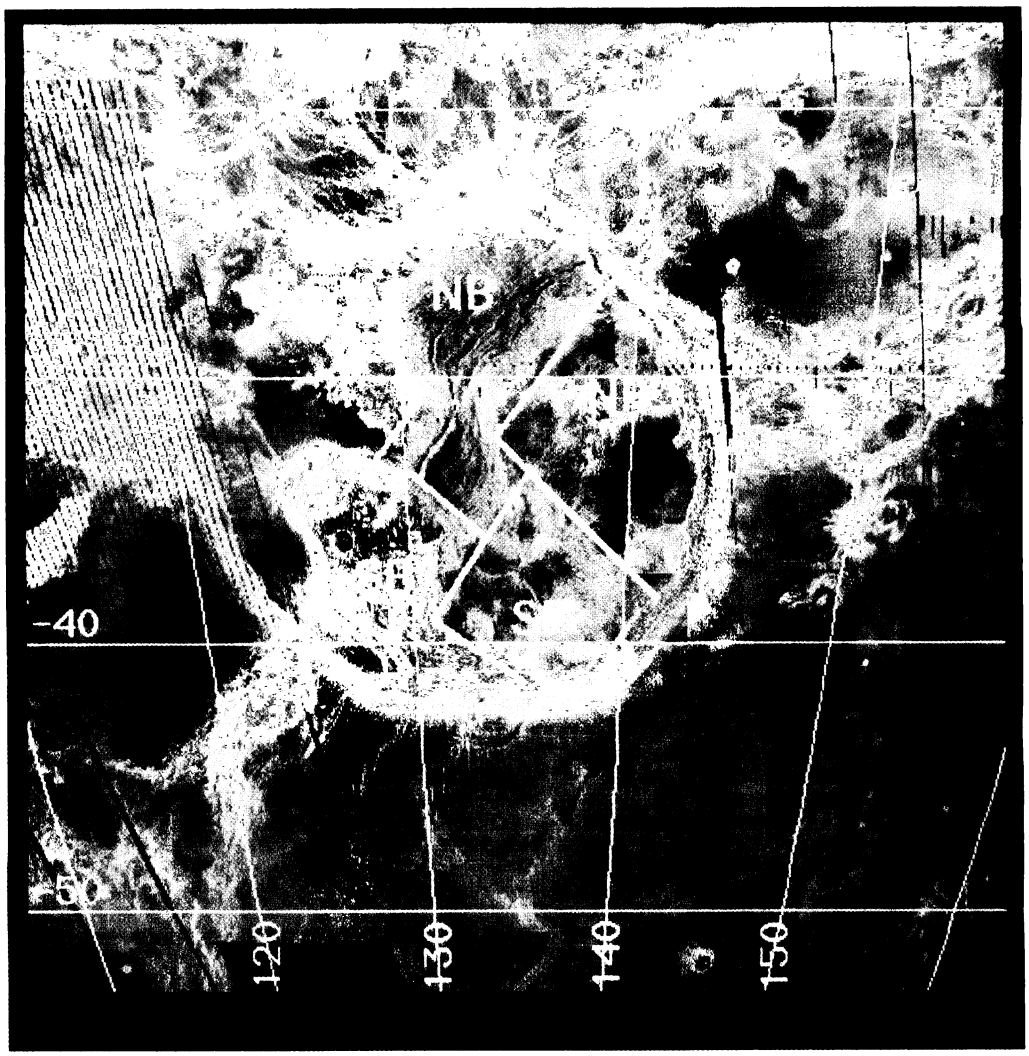

FIG. 5. Magellan SAR of Artemis Corona showing interior subregions referred to in the text. NP, northern plateua, SP, southern plateau; NB, northern deformed belt; SB, southern deformed block. The bright lineations on the upper edge of the image are Dali Chasma. Artemis Chasma forms the circular boundary of the corona.

Within the northern block (NB) there is an offset to the southeast of the northeast–southwest trough trends. To the southwest of the offset there is a very steep and narrow trough–ridge pair that terminates at the trench bounding the northeast border of the southern block (SB). The northeast–southwest structural trends prominent in the northern block (NB) continue, after interruption by the southern deformed block (SB), in the form of a northeast–southwest-trending chasma in the plains to the southwest of Artemis Corona. It is not clear whether the region to the northwest of the deformed belt (NB and SB) is a part of Artemis Corona. This region is similar to the northern plateau (NP), with smooth elevated topography and relatively little deformation of the surface flows.

The purpose of this subdivision of the interior of Artemis Corona is to provide a framework for the description of the gravity field over this large feature. According to the spherical harmonic gravity field (Fig. 1C), Artemis Corona has a large semicircular positive anomaly associated with and generally inboard of the trench. This anomaly is most prominent along the southeastern margin and peaks at 42 mgal (compared with the regional average of 7.1 mgal, Table I) over the easternmost portion of the northern plateau (NP) section; it also covers the southern plateau (SP) at values of 20–40 mgal. The southern deformed block (SB) is a region of transitional gravity signal between higher values near the corona rim and lower values in the corona interior. The prominent ridge–trough structure in the northern block (NB) is the site of a 10-mgal gravity low. Over the rest of the northern deformed region (NB) the gravity anomaly rises from low values near the center of the corona to high values over

the corona rim and the high topography marking the intersection of Diana and Artemis Chasmata. The intersections of chasmata are, in general, coincident with positive gravity anomalies. The junction of Artemis Chasma in the southwest with the southwestward-trending chasma in the plains and the intersection of Artemis Chasma with an eastward trending chasma are both sites of ≈30-mgal positive anomalies. Artemis Corona expresses itself in the geoid (Fig. 1B) as a southward extension of the broad high associated with Thetis Regio.

2.2. *Latona Corona*

Latona Corona lies within the complex Diana and Dali Chasmata system. The corona itself is defined by two semicircular asymmetric trenches which link up on the east and west with the chasmata system and may be interpreted as oppositely directed, arcuate segments of the two chasmata. The area enclosed by these trenches is ≈800 km across and contains two (perhaps three) shorter trench arcs (Fig. 1E) and a complex fracture pattern (Fig. 1H). The northern rim is extremely high, rising as much as 6 km from the bottom of the bounding trench. Its brightness in the SAR (Fig. 1H) is due to the formation of high-reflectivity material on the elevated surface (Tyler *et al.* 1991, Pettengill *et al.* 1992). The southern bounding rim is also quite high, and the outer rise that encircles the trench is the site of prominent circumferential fractures similar to those at many other coronae.

The strong, nearly east–west trend of the chasmata (Fig. 1H) is also evident in the geoid (Fig. 1F) and in the topography as a long-wavelength ridge (Fig. 1E). The long-wavelength character of the gravity field at Latona Corona is better seen in the geoid (Fig. 1F) than in the gravity (Fig. 1G). A large (≈52 m) geoid peak sits over the northern portion of the corona interior. The gravity anomaly (Fig. 1G) associated with this geoid high reaches 49 mgal (Table I). Outside the corona there are two smaller gravity highs, one to the southwest (27 mgal) associated with the junction of the southern bounding trench with another arcuate segment of the chasmata system and the other to the east (38 mgal) located over a fairly smooth region of plains-type flows. There is also evidence of the outer rise of the southern trench in the gravity map (Fig. 1G) where a lobe of the major positive anomaly crosses the trench.

2.3. *Coronae in Eastern Eistla Regio*

Eastern Eistla Regio is the site of a group of four unusual coronae including Pavlova Corona. The coronae in this group are each 300–400 km in diameter and are arranged at the corners of a rectangular area of elevated topography (Fig. 2A); Pavlova Corona (400 km in diameter) is on the southwest corner. A concentric, double-ring corona (Stofan *et al.* 1992) with less topographic expression lies to the south of the group. Between Pavlova Corona and the southeastern member of the group is a circular region of deformation that could be a heavily tectonized corona. The four coronae are unusual in two respects: the lack of even a partial moat encircling the features and the nature of the peripheral fracture patterns. These fracture patterns (Fig. 2D) occur on the tops of the high circular rims of the coronae and are made up of very fine lineaments trending radially away from the radially fractured central topographic highs. The prominent radial trend of the central topographic high and rim fractures and the absence of radial fractures in the coronae interiors suggest that radial fractures in the interior have been embayed by material that did not breach the rim or bury the central topographic high.

All four coronae are coincident with positive gravity anomalies (Fig. 2C) with a maximum anomaly over the northwestern corona of 45 mgal and 40-mgal peaks over Pavlova Corona and the southeastern corona (Table I). The less distinct (topographically and in the SAR) northeastern corona has a 35-mgal anomaly. Bell Regio is apparent at the northern edge of the region, and three mid-sized volcanoes to the southwest of the group are identifiable in both the topography (Fig. 2A) and the gravity field (Fig. 2C). The corona to the south of the group is not associated with any gravity anomaly. Meade Crater (280 km diameter) to the east of the group coincides with a lobe of the elongated gravity lows to the northeast. This region of low gravity and another region of gravity lows to the west of the corona group are associated with chasmata/rift features.

There is a broad region of positive geoid height anomaly (Fig. 2B) associated with the elevated topography of the corona group. Within this region of geoid high there is a local maximum over Pavlova Corona and the northwestern corona. Bell Regio also has a prominent positive geoid height anomaly.

2.4. *Segments of Parga, Western Parga, and Hecate Chasmata*

The regions including arcuate segments of Parga, Western Parga, and Hecate Chasmata that we have studied (Figs. 2–3) have also been identified as coronae (Stofan *et al.* 1992). Topographically, these three chasmata regions are very similar (Figs. 2E, 3A, 3E) and bear a strong resemblance to Latona Corona (Fig. 1E) which is twice as large. In each region, a portion of the asymmetric trench in the chasma curves sharply to define part of the corona's boundary. The remaining boundary of the corona is defined by tectonic lineations visible in the SARs (Figs. 2H, 3D, 3H) that correspond to a trench at Hecate and Western Parga Chasmata, and an elevated

rim in the case of Parga Chasma. These strongly curved chasmata segments often occur where the topographic asymmetry of the trench reverses, most clearly seen at Parga Chasma (Fig. 2E). In each location, the interior of the corona contains a radial set of fractures that are most prominent at Hecate Chasma (Fig. 3H), where they cover the whole interior, and weakest at Parga Chasma (Fig. 2H), where flows and fractures can be seen emanating from the same point on the southern end of the corona.

At Parga Chasma, a 38-mgal positive gravity anomaly (Table I) and a small positive geoid height anomaly are associated with the corona (Figs. 2F, 2G). Although equally high topography (Fig. 2E) occurs on the other side of the chasma to the east, there is a much smaller positive anomaly (≈20 mgal) there. There are many other coronae in this chasma region, such as the large half-circle corona to the southeast and the smaller radial corona to the north, which are also coincident with positive gravity anomalies. None of these other anomalies is much more than half of the large gravity anomaly at the central corona, however.

At Western Parga Chasma, the elevation of the northern rim of the corona reaches 5 km above the curving trench that defines the northern border (Fig. 3A). The southern trench is much less well defined, although the scarp is quite visible in the SAR (Fig. 3D). Also visible in the SAR is the centrally located radial fracture pattern which, as at Parga Chasma, also seems to be the origin of the interior lava flows. A 49-mgal positive gravity anomaly (Table I) is centered right over the corona (Fig. 3C). The corona is also the site of a lobe on the shoulder of the broad geoid anomaly associated with Atla Regio (Fig. 3B). The large radial corona to the north is associated with a 26-mgal positive anomaly, but none of the other features in the region have counterparts in the present spherical harmonic representation of the gravity field. In particular there is no gravity anomaly associated with the high topography along the chasma to the northwest.

The corona at Hecate Chasma (Fig. 3E) is bounded on the north and south by deep trenches which merge on the western side to form a straight region of asymmetric chasma 1000 km long. This straight section of chasma can be sharply contrasted to the curved section defining the corona when one looks at the gravity field (Fig. 3G). The corona is the site of a 38-mgal positive anomaly (Table I) while the anomaly over the straight chasma section is only ≈15 mgal. Another region of curved trenches and uplifted corona rims can be seen on the western side of the area in Fig. 3E; this area corresponds to a ≈37-mgal positive anomaly. The elevated topography and the large positive gravity anomaly to the northeast of the corona are on the western flank of Beta Regio. This part of Hecate Chasma concides with a ridge of near zero geoid that breaks the ring of low geoid surrounding the high at Beta Regio (Fig. 3F).

2.5. *Plains Coronae*

Although many coronae are associated with the chasmata of Venus, there are some which lie in the plains far from either chasmata or volcanic rises. Two of these, Heng-o Corona (1060 km diameter) and Fatua Corona (310 km diameter), are associated with positive gravity anomalies and we have included them in our study.

Heng-o Corona is a very large feature in Tinatin Planitia between western Eistla Regio and Alpha Regio. The topography of Heng-o Corona (Fig. 4A) is relatively subtle, the most notable features being the volcano in the western interior, the northern rim, and the broad southern outer rise. The gravity field in this region (Fig. 4C) peaks at ≈20 mgal over the southern outer rise at its eastern end, and a region of high gravity follows the outer rise around the southeastern margin of the corona. A second gravity high (≈18 mgal) is associated with a gently domed region in the southwest of the corona's interior, corresponding to a region of northwest–southeast-trending fractures in the SAR (Fig. 4D). No gravity features corresponding to the interior volcano or the northern rim are seen. Heng-o Corona has little expression in the geoid (Fig. 4B). The topographic and gravity highs to the north of Heng-o Corona represent the southern flank of the volcanic rise in western Eistla Regio.

Fatua Corona lies 2500 km to the southeast of Heng-o Corona, in the same plains region (Tinatin Planitia). The interior of Fatua Corona is elevated as much as 2.5 km above the surrounding plains (Fig. 4E), with a bowl-like shape to the interior plateau. There is a trough that encircles the corona, and an outer rise exterior to this trough that is highest on the southwest. There is a double set of circumferential fractures evident in the SAR (Fig. 4H) that interact with a nearly north–south set of fractures corresponding to a trough that cuts the outer rise on the south side of the corona (Fig. 4E). The gravity anomaly at Fatua Corona (Fig. 4G) has a local maximum (22 mgal) overlapping the northern part of the corona which is part of an elongated positive anomaly with a second maximum over an unusual circular structure (Figs. 4E, 4H) to the northwest. Fatua Corona coincides with a lobe on a geoid slope that descends northward into the plains (Fig. 4F).

3. INTERPRETATION

3.1. *Apparent Depths of Compensation*

Best fit apparent depths of compensation (ADC) have been derived for all of the features studied in this paper from the topographic data of a feature, a simple Airy-like

lithospheric thinning or thermal isostasy model, and visual comparison with the prominent gravity anomaly associated with the feature (using the spherical harmonic gravity field). The linear transfer function $Q(k)$ for the surface free-air gravity produced by topography compensated at mean depth ADC is

$$Q(k) = 2\pi\rho G(1 - e^{-k(\mathrm{ADC})}), \quad (1)$$

where ρ is the density above the ADC and k is the horizontal wavenumber of the Fourier transform of the topography. Here it is assumed that the compensating interface at average depth ADC has a sufficiently high density contrast so that the vertical excursions of the interface are much less than the mean compensation depth. However, if the density variations are small a nonlinear model (Parker 1973) may be more appropriate. This nonlinear effect may be apparent in plots of geoid height vs topography (Turcotte and Schubert 1982, Moore and Schubert 1994).

Forward models of the Fourier transform of the regional gravity are calculated from the Fourier transform of the Magellan topography of the region and Eq. (1). Spatial gravity maps are obtained from the inverse Fourier transform of the model gravity field in the wavenumber domain. Gravity models are constructed for ADCs from 25 to 200 km at intervals of 25 km and the best model is determined by comparison of the amplitude of the prominent model gravity anomaly of a feature with the amplitude of the prominent observed gravity anomaly. The best fit ADC is therefore constrained only to within ± 12.5 km and represents the compensation depth of the prominent gravity feature and not a regional compensation depth. The ADCs are reported in Table I and discussed below.

3.1.1. *Artemis Corona.* The best fit ADC to the large gravity anomaly along the southeastern margin of Artemis Corona (Fig. 1C) is about 200 km (Table I). The best fit ADC for the Artemis region in general is much smaller, about 50 km, although an Airy-like model with a single depth of compensation does not provide a particularly good representation of the regional gravity. The large depth of compensation of the major gravity signal associated with Artemis Chasma implies either a very thick lithosphere inboard of the trench if the gravity anomaly is caused by the topographic ridge at this location or a deep positive mass anomaly inboard of the trench if the topographic ridge is actually compensated at shallow depth. The small ADC of the region in general would suggest relatively shallow compensation of topography and a deep positive mass anomaly as the source of the gravity high.

3.1.2. *Latona Corona.* The major gravity high over Latona Corona (Fig. 1G) has a best fit ADC of about 150 km (Table I), essentially as deep as the ADC of the gravity high over the southeastern margin of Artemis Corona. The good correlation of topography with gravity over Latona Corona suggests that the gravity high over the northern half of the corona might in fact be caused by the topographic ridge inboard of the northern trench. Such an interpretation, together with the ADC of 150 km, would require that the lithosphere be about 150 km thick at the location of the corona. While this may be plausible, an alternative interpretation of the deep ADC is that the gravity high is actually caused by a deep mass anomaly inboard of the northern chasm of Latona Corona and the topography is compensated at shallower depths.

3.1.3. *Coronae in Eastern Eistla Regio.* The four coronae in this group have a best fit ADC of about 75 km (Table I), small compared to the ADCs of Artemis and Latona Coronae and the ADC ($\approx$125 km) of nearby Bell Regio (see also Smrekar 1994). The excellent correlation of gravity and topography over these coronae (Figs. 2A, 2C), together with their relatively shallow ADC, support the interpretation that the topography of the coronae are directly responsible for their gravity anomalies and the topography is compensated at the base of a crust or lithosphere about 75 km thick.

3.1.4. *Segments of Parga, Western Parga, and Hecate Chasmata.* The ADC of the corona in Parga Chasma (Fig. 2) is about 125 km, the ADC of the corona in western Parga Chasma (Fig. 3) is about 75 km, and the ADC of the corona in Hecate Chasma (Fig. 3) is about 150 km (Table I). Again possible interpretations involve gravity anomalies due to the uplifted chasmata flanks with lithosphere thicknesses of 75 to 150 km in the individual cases or relatively shallow compensation of chasmata flank topography with gravity highs due to mass anomalies buried at depths of 75 to 150 km. The association of the gravity anomalies with only the concave sides of arcuate chasma segments together with the absence of similarly high gravity anomalies over other portions of the same chasma with equally high standing topography argue for a buried mass anomaly as the source of the gravity signal. Also, the negative gravity anomaly of the chasma itself (not observed) must compensate the positive anomaly of the uplifted chasma flanks.

3.1.5. *Plains Coronae.* The best fit ADC for the gravity high near the southern margin of Heng-o Corona (Fig. 4) is 150 km (Table I), about as large as the ADCs of the gravity highs over the southeastern margin of Artemis Corona and the northern half of Latona Corona. Such a large ADC is consistent with a topographic origin for the gravity field and a very thick lithosphere beneath Heng-o Corona; it is also consistent with total or partial compensation of topography at shallow depth (a thinner lithosphere or crustal compensation of topography) and a

deep positive mass anomaly as a source of the gravity signal. Heng-o Corona is a relatively subdued or degraded corona, presumably in a late stage of its evolution (Stofan and Head 1990, Stofan *et al.* 1992, Squyres *et al.* 1992, Sandwell and Schubert 1992a), so a thick lithosphere (though not necessarily as thick as 150 km) beneath Heng-o Corona is likely. The topography along the northern margin of Heng-o Corona is typical of a flexural outer rise exterior to a tectonically deformed moat, and the inferred elastic thickness (40 km) of the exterior plate is consistent with an old, thick lithosphere (Sandwell and Schubert 1992a). The coincidence of the gravity high with the outer rise on the southern margin of Heng-o Corona (*Fig. 4C*) is also suggestive of a flexural origin for this feature since flexural topography will appear deeply compensated.

Fatua Corona (Fig. 4) has a smaller ADC (75 km, Table I) than the much larger Heng-o Corona, suggesting that either the lithosphere beneath Fatua Corona is thinner, or that most of the gravity anomaly arising from this 300-km-diameter corona is unresolved. The higher amplitude of topography at Fatua Corona (Fig. 4E) compared with that at Heng-o Corona (Fig. 4A) (which is largely responsible for the lower ADC of Fatua Corona since the gravity anomalies of the two coronae are equal) is also consistent with a younger, thinner lithosphere. Flexural studies of Fatua Corona (not reported here) yield elastic plate thickness estimates smaller than that at Heng-o Corona in further support of a thinner lithosphere beneath Fatua Corona.

3.1.6. *Comparison of Corona ADCs.* The ADCs of the regions studied are plotted against the size of the gravity feature in Fig. 6. In most cases the size of the geologic feature and its expression in the gravity field are the same. However, this is not the case for Heng-o and Artemis Coronae. The prominent gravity anomaly at Artemis Corona is associated only with the southeastern margin of the corona and the size of the gravity anomaly is accordingly smaller than that of the entire corona. The gravity anomaly at Heng-o Corona is mainly associated with the outer rise on the southern margin of the corona.

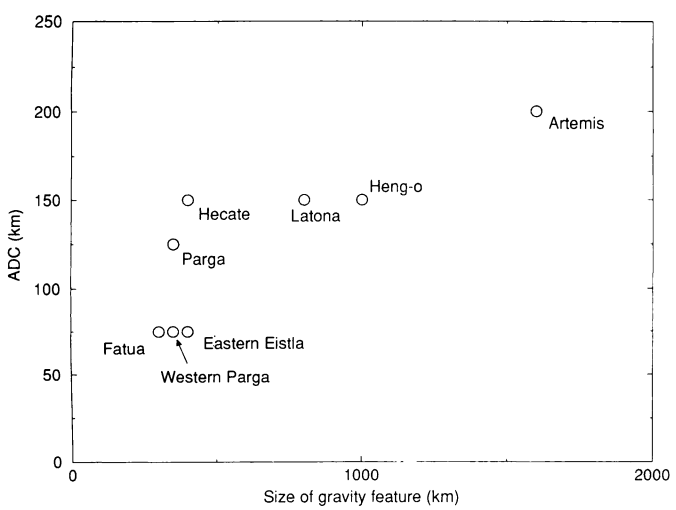

FIG. 6. Apparent depth of compensation (ADC) derived from the best fitting Airy-like model of topographic compensation plotted against the size of the gravity feature to which the fit was made.

The ADCs of Heng-o and Latona Coronae and the southeastern quadrant of Artemis Corona are similar (150–200 km) though the gravity features differ in size by a factor of two. There is a factor of two difference in the ADCs of the coronae in Hecate and Parga Chasmata (≈150 km) and the coronae in western Parga Chasma and eastern Eistla Regio and Fatua Corona (≈75 km), which are all about the same size. Overall, there is a tendency for the ADC to increase with the size of the gravity feature although this trend has the obvious exceptions noted above. The ADCs of Heng-o, Latona, and Artemis Coronae (150–200 km) are comparable to the ADCs of the major volcanic rises Atla and Bell Regiones (Smrekar and Phillips 1991, Smrekar 1994); only Beta Regio has a significantly larger ADC (Smrekar and Phillips 1991, Moore and Schubert 1994). The large coronae ADCs (75–200 km) argue against compensation at a crust–mantle interface or Moho (the thickness of the basaltic crust on Venus is limited by the basalt–eclogite transition to be less than about 75 km; Anderson 1981, Turcotte 1989) and instead argue for compensation by a thick lithosphere (of variable thickness) or by dynamic mechanisms associated, in the cases studied here, with possible lithospheric subduction or underthrusting (Sandwell and Schubert 1992a, b).

3.2. Gravity/Topography and Geoid/Topography Ratios

The gravity/topography ratio (GRTR) and the geoid/topography ratio (GTR) are alternative quantitative measures of the degree to which topography is expressed in the gravity field or geoid. The GRTR and GTR for the Airy-like transfer function given in (1) are

$$\text{GRTR} = Q(k) = 2\pi\rho G\{1 - e^{-k(\text{ADC})}\} \tag{2}$$

$$\text{GTR} = \frac{2\pi\rho G}{g}\left\{\frac{1 - e^{-k(\text{ADC})}}{k}\right\}. \tag{3}$$

For wavelengths ($\lambda = 2\pi/k$) sufficiently long that $k(\text{ADC}) \ll 1$, the GRTR and GTR simplify to

$$\text{GRTR} = 2\pi\rho G k(\text{ADC}) \tag{4}$$

$$\text{GTR} = \frac{2\pi\rho G(\text{ADC})}{g}. \tag{3}$$

For wavelengths between 600 and 4000 km it is possible to evaluate the GTR in the spatial domain since (5) is a reasonable approximation to the GTR (Sandwell and Renkin 1988). This allows investigation of irregularly shaped regions and also permits the determination of the spatial variation of the GTR over the surface (*see also* Simons *et al.* 1994). Though the GRTR is weakly dependent on wavelength (see (4)), the limited bandwidth (600 km to 4000 km) also makes it possible to evaluate the GRTR in the spatial domain.

In order to remove wavelengths longer than 4000 km from both the topography and the geoid height (gravity) datasets, we subtracted both the mean and the best-fit plane for a study region between 1800 and 4000 km across. Wavelengths shorter than 600 km were removed by convolution with the Gaussian filter

$$f(r) = \exp\left(\frac{-r^2}{\sigma^2}\right), \tag{6}$$

where σ = 180 km and r is the distance between two observations (Sandwell and Renkin 1988). This smooth filter prevents aliasing of short-wavelength power into the wavelength band of interest. The geoid height (gravity) and topography data were then sampled at a horizontal resolution of 3° (315 km) to assure linear independence of the data. The geoid height (gravity) and topography data at each point were then plotted against each other and the GTR (GRTR) was calculated via nonbiased linear regression (Marks and Sandwell 1991). A nonbiased technique was employed rather than the straightforward least-squares formulation because the distributions of measurement errors in the geoid (gravity) and topography datasets are unknown. In this case, an unbiased estimate of the slope can be obtained by minimizing the sum of the squares of both topography and geoid (gravity) differences between the observations and the model. This slope is always greater than that obtained by least-squares regression of geoid (gravity) vs topography in which all measurement errors are assumed to be in the geoid (gravity) observations. One-sigma error bars are obtained by determining the $\Delta\chi^2 = 1$ (68.3%) confidence interval of the minimized sum.

The results of these calculations are plotted in Figs. 7 and 8 and given in Table I. The GTRs for Latona and Artemis Coronae, the coronae in Eastern Eistla Regio, and Hecate Chasma are well determined; the GTRs for the coronae in Parga Chasma and western Parga Chasma and Heng-o and Fatua Coronae are less well determined. The GRTRs for Latona and Artemis Coronae and the coronae of Eastern Eistla Regio are well constrained by the data in Fig. 8, while the GRTRs of Heng-o and Fatua Coronae, and the coronae in western Parga Chasma, Parga Chasma, and Hecate Chasma are less well constrained.

The GTRs of the different regions are plotted together in Fig. 9 versus wavelength; a wavelength is assigned to each GTR determination equal to the width of the region studied. Error bars are the one-sigma uncertainties listed in Fig. 7 and Table I. The GTR of Atla Regio (determined by us, see also Smrekar and Phillips 1991, Phillips *et al.* 1991) has been included in Fig. 9 to emphasize that the GTRs of Latona, Artemis, and Heng-o Coronae are about as large as the GTRs of the major volcanic rises. Also plotted in Fig. 9 are theoretical GTRs according to (3) for different values of ADC. All the GTRs require compensation at depths in excess of 75 km. Because of these large compensation depths, it is highly unlikely that these features could be compensated at a Moho or crust–mantle boundary. It is more likely that compensation is due to thickness variations of a thick lithosphere or to deep-seated dynamical processes. There is a tendency for smaller features to have smaller GTRs, in accordance with the tendency of smaller features to have smaller ADCs (Fig. 6). The differences between the ADCs one would infer from Fig. 9 and those given in Table I probably result from the action of the spatial filters and the emphasis we placed on major gravity peaks when comparing the forward Airy-like models with the gravity observations.

The GRTRs are shown in Fig. 10 together with the theoretical GRTRs according to (2) for different values of the ADC. The ADC of Latona Corona inferred from Fig. 10 is smaller than the ADC deduced from Fig. 9. These ADCs are comparable for Atla Regio and Artemis, Fatua, and Heng-o Coronae. For the coronae in Hecate, Parga and western Parga Chasmata, and the coronae in Eastern Eistla Regio, the ADC from the GRTR is somewhat larger than the ADC from the GTR. These ADC differences are due to the greater emphasis the GRTR (GTR) places on shorter (longer) wavelengths. For example, the strong correlation of short wavelength topography and gravity over the coronae at eastern Eistla Regio (Figs. 2A, 2C) is responsible for the somewhat larger ADC inferred from the GRTR, while the strong correlation of long-wavelength topography and gravity at Latona Corona causes the larger ADC inferred from the GTR. The differences between Figs. 7 and 8 are also due to this wavelength dependent effect.

The GTRs and GRTRs for the group of coronae with the smaller ADCs are plotted versus long-wavelength topographic height in Fig. 11 (GRTR/k is actually plotted, see below). For Airy-like compensation of topography, GTR and GRTR depend on topographic height h according to (Turcotte and Schubert 1982)

$$\mathrm{GTR} = \frac{2\pi G\rho_c H}{g} + \frac{\pi G\rho_c}{g}\left(\frac{\rho_m}{\rho_m - \rho_c}\right) h \tag{7}$$

$$\frac{\mathrm{GRTR}}{k} = g(\mathrm{GTR}), \tag{8}$$

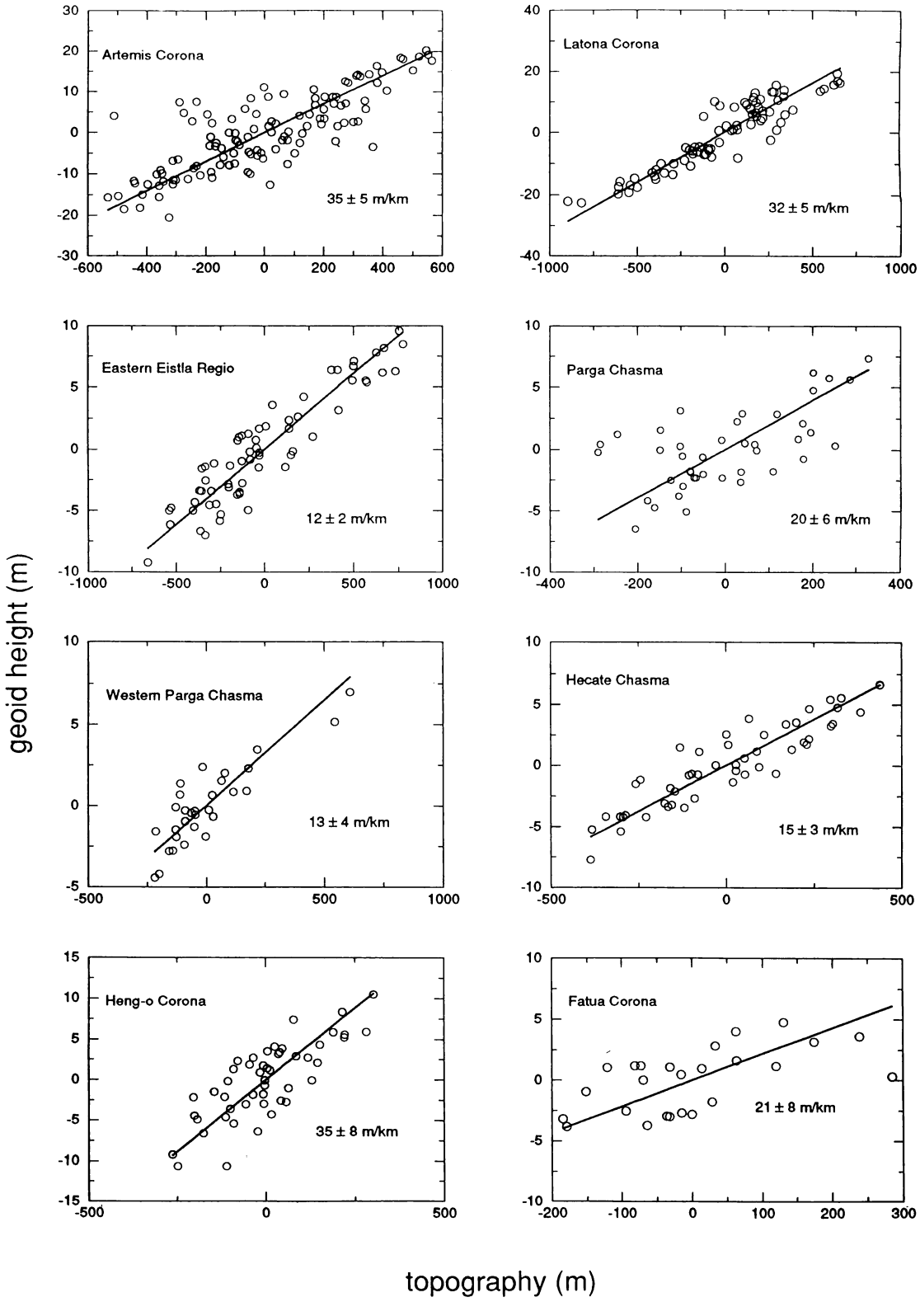

FIG. 7. Geoid height (m) vs topography (m) for data averaged over 3° squares in the eight study regions. The slope of the nonbiased linear fit is the geoid/topography ratio (GTR) given on the figure and in Table I.

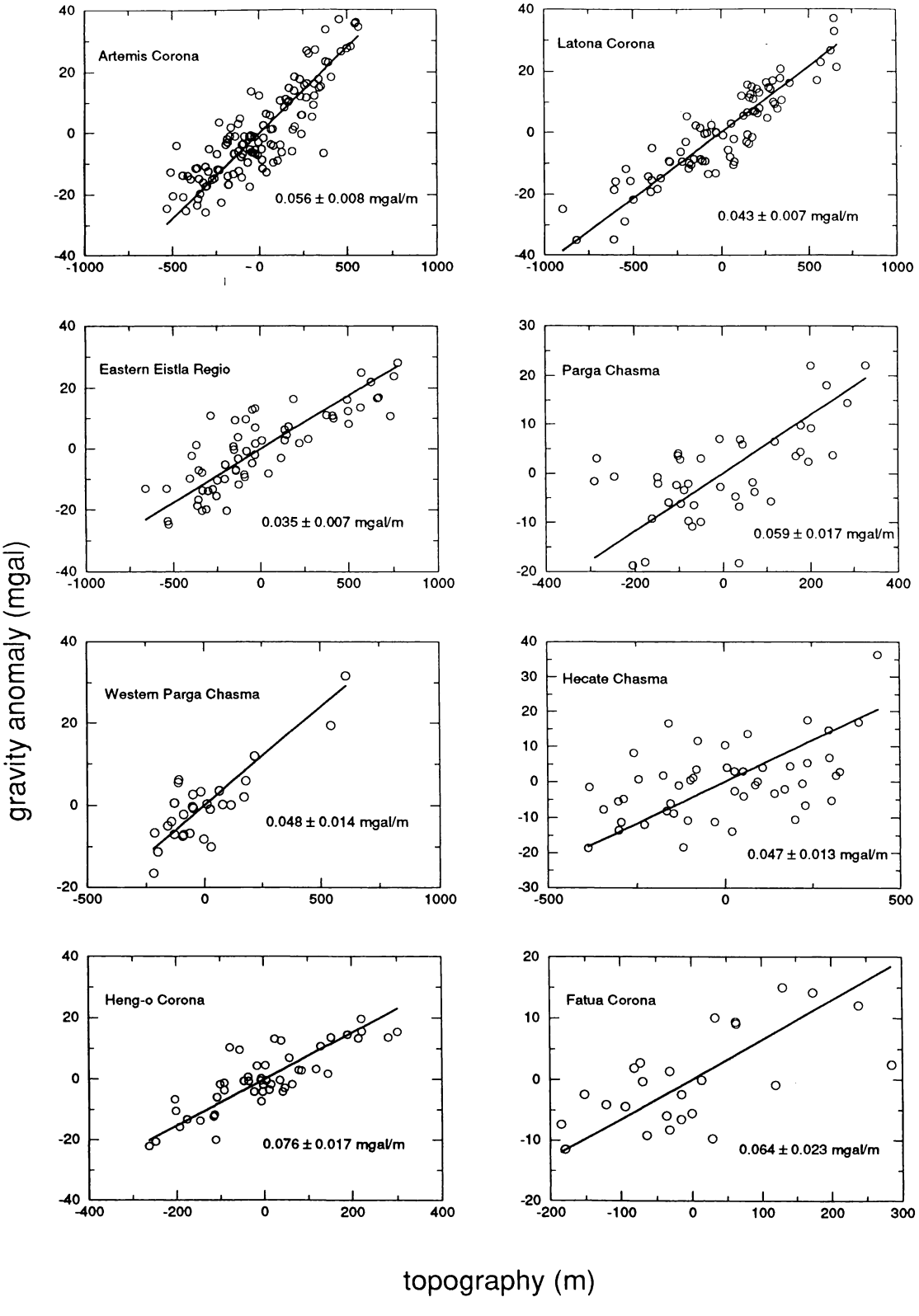

FIG. 8. Similar to Fig. 7 except for the gravity anomaly and the GRTR.

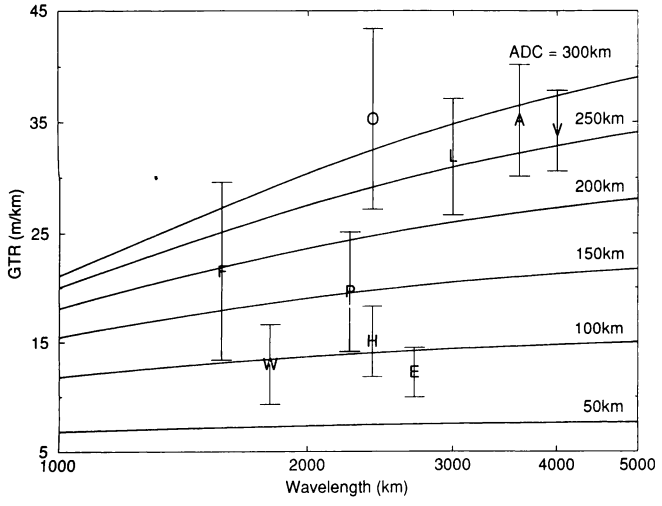

FIG. 9. Geoid height/topography ratio (GTR) versus wavelength for the coronae and chasmata features studied in this paper. A, Artemis Corona; L, Latona Corona; E, coronae in eastern Eistla Regio; P, Parga Chasma; W, western Parga Chasma; H, Hecate Chasma, O, Heng-o Corona, F, Fatua Corona. The GTR for Atla Regio has also been plotted and is designated V. The curves are the theoretical GTRs according to (3), labeled with the value of the ADC.

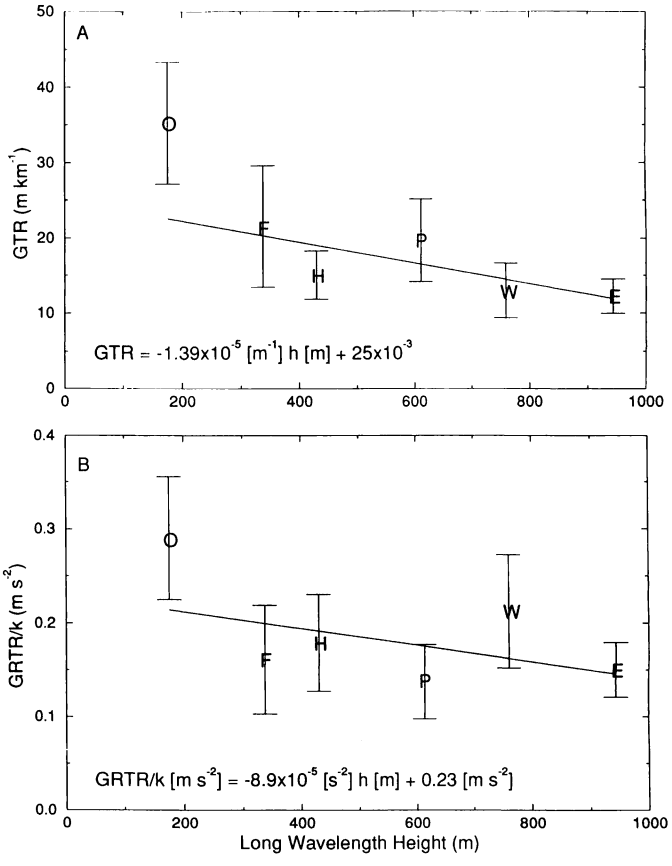

FIG. 11. GTR (A) and GRTR (B) versus long wavelength height (Table I) for Heng-o Corona (O), Fatua Corona (F), four coronae in eastern Eistla Regio (E), and arcuate segments of Hecate (H), Parga (P), and western Parga (W) Chasmata. The straight lines are weighted linear least squares fits to the data. The negative slopes of these lines are consistent with compensation of these features by thickness variations of a dense lithosphere overlying a less dense mantle. The slopes and intercepts of these lines are interpreted in the text to yield average lithosphere thickness and excess lithosphere density.

where ρ_c and H are the upper layer density and average thickness, respectively, and ρ_m is the underlying mantle density. From (7) and (8), observed values of GTR and GRTR/k should depend linearly on h, and the weighted least squares fits to the data of Fig. 11 are consistent with this dependence. The best-fit slopes are negative; from (7) this implies $\rho_c > \rho_m$. Accordingly, compensation must occur by temperature-induced thickness variations in a more dense lithosphere overlying a less dense mantle. The intercepts of the best-fit linear relations on the GTR and GRTR/k vs h plots give average lithosphere thicknesses of $H = 176 \pm 28$ km and $H = 183 \pm 40$ km, respectively. The slopes of the best fit lines give lithosphere–mantle density differences $(\rho_c - \rho_m)/\rho_m = 0.51 \pm 0.22\%$ and $0.71 \pm 0.56\%$ for the GTR and GRTR/k relations, respectively. These density differences are consistent with thermal compensation of topography by mantle temperature anomalies of about 200 K. Similar density differences between the lithosphere and sublithospheric mantle have been inferred for the compensation of Beta Regio by lithosphere thinning (Moore and Schubert 1994).

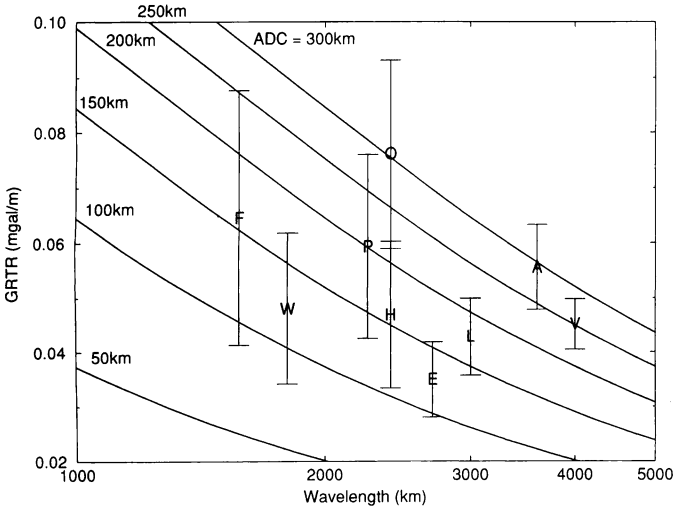

FIG. 10. Similar to Fig. 9 but for the gravity/topography ratio GRTR.

3.3. *Comparison between Intermediate Wavelength Gravity Anomalies of Venusian Chasmata and Terrestrial Subduction Zones*

Based on morphological and topographic similarities between certain segments of venusian Chasmata and ter-

restrial subduction zone arcs, Sandwell and Schubert (1992a, b) have suggested that retrograde lithospheric subduction could be occurring on Venus. In particular, they identified the southeast margin of Artemis Corona and the southern margin of Latona Corona as possible subduction trenches. In a further study of possible subduction zone sites, Schubert and Sandwell (1994) have also identified the northern margin of Latona Corona and segments of Parga and Hecate Chasmata as places where the venusian lithosphere is subducting. We propose here that the chasmata-associated gravity highs on Venus constitute additional support for subduction at these sites.

In Fig. 12 we compare the intermediate wavelength (600 km–several thousand kilometers) gravity anomalies (from the spherical harmonic model) over Artemis Corona with the gravity anomalies of similar wavelengths (also from a spherical harmonic model; Rapp and Pavlis 1990) over the Aleutians and the Marianas. A comparison of gravity anomalies over Latona Corona and the Sandwich arc is also shown in Fig. 12. The prominent terrestrial gravity anomalies are on the concave sides of the arcs and are known to be due in large part to the subducted slabs beneath the arcs (McAdoo 1981). The gravity anomalies of venusian Chasmata are also on the concave sides of the arcuate portions of the chasmata and the large depths of compensation of these gravity features and their large GTRs and GRTRs are consistent with their origin being due to subducted lithosphere.

Though we know that subduction is occurring along the terrestrial arcs, intermediate wavelength gravity anomalies are not prominent everywhere along the arcs. The intermediate wavelength gravity field is also influenced by other mass anomalies, e.g., variations of lithosphere thickness and ocean depth transverse to the arcs and back-arc spreading. Thus it is not necessary, or even surprising, for intermediate wavelength gravity anomalies to not be prominent everywhere along a chasma at which subduction might be occurring. Conversely, the

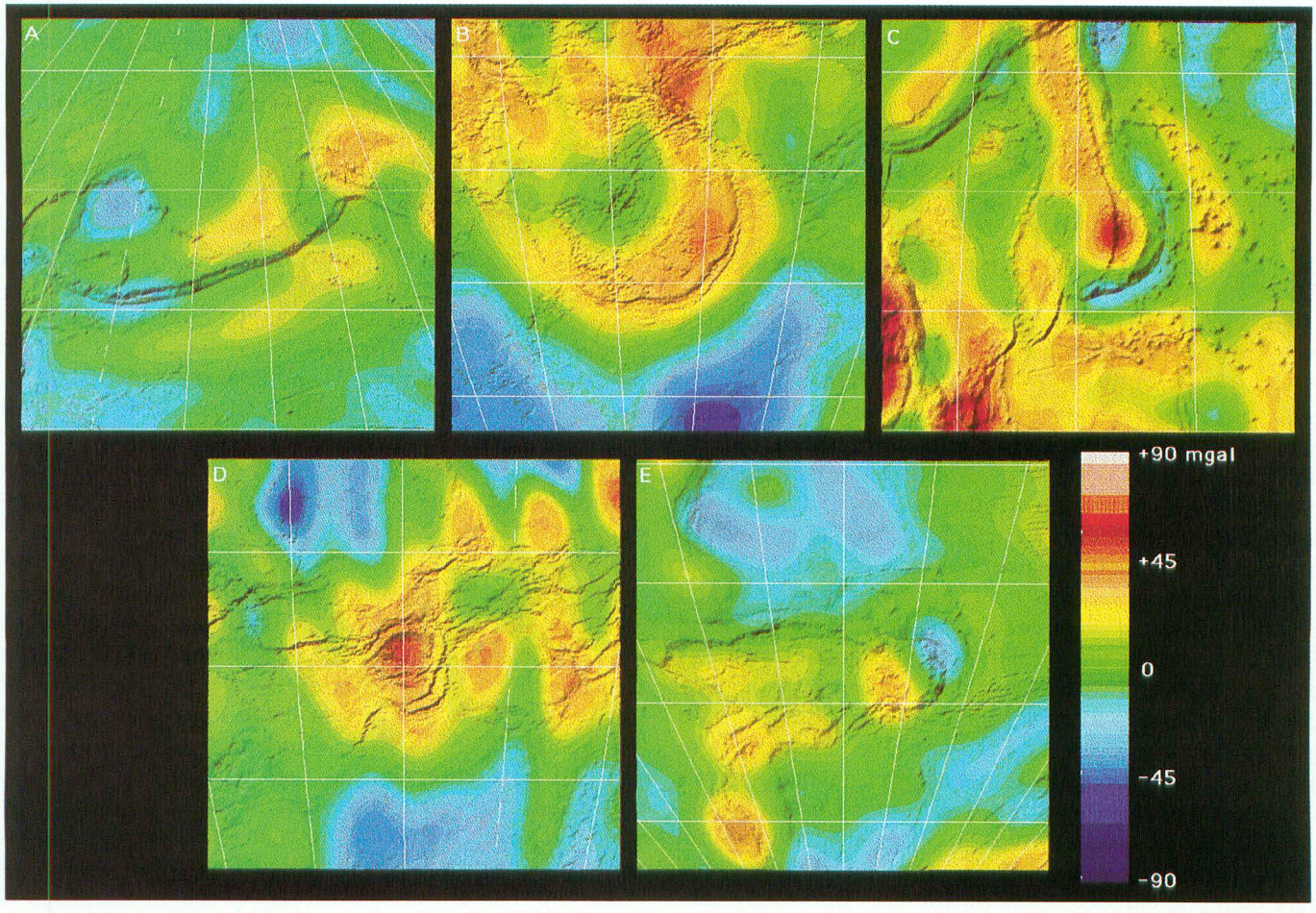

FIG. 12. Spherical harmonic gravity fields of Earth and Venus over (A) the Aleutian Trench, (B) Artemis Corona, (C) the Marianas Trench, (D) Latona Corona, and (E) the Sandwich Trench. Earth's gravity field is a 60th degree smooth truncation of the 360th degree and order field of Rapp and Pavlis (1990). The Venus gravity field is the MGNP60FSAAP model of Konopliv and Sjogren (1994).

TABLE II
Gravity Data over Earth and Venus Trenches

Feature	Planform radius [km]	ADC [km]	GTR [m/km]	GRTR [mgal/m]	Subduction angle [deg][a]
Sandwich Trench	400	40	5.9 ± 1.0	0.013 ± 0.002	70
Aleutian Trench	1200	25	3.2 ± 0.6	0.008 ± 0.002	60
Marianas Trench	1000	70	−5.1 ± 2.3	0.010 ± 0.002	90
Artemis Chasma	1200	200	35 ± 5	0.056 ± 0.008	?
Latona Corona	400	150	32 ± 5	0.043 ± 0.007	?

[a] Subduction angles taken from Uyeda and Kanamori (1979).

existence of such a gravity anomaly adjacent to an arcuate segment of a chasma is not proof in itself of subduction at the site.

Application of the same technique we use to obtain best fit ADCs of venusian gravity anomalies to the terrestrial subduction zone anomalies gives the results shown in Table II. The ADCs of the terrestrial anomalies are generally shallower than those of the chasmata-associated gravity anomalies on Venus. The GTRs and GRTRs for the terrestrial subduction zones are generally lower than their venusian counterparts. The GTR for the Marianas trench is not well determined due to lack of correlation between gravity and topography in this region.

4. DISCUSSION AND CONCLUDING REMARKS

The gravity signals of coronae and arcuate segments of chasmata support the idea that there may be two distinct types of coronae with fundamentally different origins—relatively small coronae several hundred kilometers across arising from plume-like or diapiric mantle upwellings (Stofan *et al.* 1991, Janes *et al.* 1992) or melt instabilities in broadly upwelling mantle (Tackley and Stevenson 1991, 1993, Tackley *et al.* 1992) and coronae of all sizes formed from arcuate segments of chasmata along which subduction or underthrusting is occurring (Sandwell and Schubert 1992a, b, McKenzie *et al.* 1992, cf. Hansen and Phillips 1993). In the former case, the gravity signal is centered over the structure as it is over each of the four coronae in eastern Eistla Regio, and in the latter case the gravity signal is located on the concave side of the arc segment, as it is along the southeastern trench of Artemis Corona and the northern trench of Latona Corona. Structures such as Latona Corona may be misidentified in a sense; i.e., the circular appearance of Latona Corona may be a coincidence of the positions of oppositely subducting or underthrusting arc segments of the Dali–Diana Chasmata system. Indeed, the opposing arc segments in Hecate Chasma shown in Fig. 3 define a structure extraordinarily similar to Latona Corona, but on a smaller scale.

The type of subduction that might be occurring along arcuate chasmata segments is retrograde subduction (Garfunkel *et al.* 1986) in which the trench migrates into the lithosphere on the convex side of the arc thereby increasing the arc radius of curvature (Sandwell and Schubert 1992b). Accordingly, Latona Corona could have reached its present size from a smaller structure analogous to the one in Hecate Chasma. The large size of Artemis Corona is also more readily explained by this process, for the alternative corona forming process would require a large mantle plume beneath Artemis Corona in which case it would be difficult to explain why Artemis Corona is not a major volcanic rise like Atla Regio and Beta Regio.

The possible occurrence of subduction along segments of chasmata requires that the subducting lithosphere be old and thick, the exact age and thickness depending on the thickness of the venusian crust (Schubert and Sandwell 1994). The large ADCs, GTRs, and GRTRs of many of the gravity signals analyzed in this paper are consistent with a thick Venus lithosphere at possible subduction sites. Analysis of flexural deformation at different locations on Venus also points to the existence of thick lithosphere in some regions (Sandwell and Schubert 1992a, Johnson and Sandwell 1994). Because the Venus lithosphere must be old and thick to subduct, the initiation of the process requires a mechanism to break the lithosphere. This mechanism could be rifting (Schubert and Sandwell 1994), which would account for the occurrence of subduction along arcuate segments of chasmata. Chasmata may originate as rifts near the centers of the major volcanic rises and propagate radially away from the rises toward lower elevations and into regions of older and thicker lithosphere. Once broken, the edges of chasmata could sink into the mantle if the lithosphere is negatively buoyant; the edge that would subduct is the one that would move downhill as the lithosphere rolls

back. Chasmata could thus have a dual nature. They could be quasi-symmetric rifts near the centers of volcanic rises and asymmetric trenches in the lowlands far from the rises (Schubert and Sandwell 1994). Rifting and subduction on Venus may be initimately related and together they might provide a mechanism for the massive overturn of the Venus lithosphere (Turcotte 1993).

In closing, we need to emphasize that the circular orbit gravity survey of Venus by Magellan is not yet complete and the final representation of the gravity field by spherical harmonics is not in hand. All interpretations of Venus gravity and topography will have to be revisited once a more detailed gravity field is available.

ACKNOWLEDGMENTS

This work was supported by NASA through the Magellan Project (JPL958496) and the Venus Data Analysis Program (NAGW 3546).

REFERENCES

ANDERSON, D. L. 1981. Plate tectonics on Venus. *Geophys. Res. Lett.* **8,** 309–311.

FORD, P. G., AND G. H. PETTENGILL 1992. Venus topography and kilometer-scale slopes, *J. Geophys. Res.* **97,** 13103–13114.

GARFUNKEL, Z., C. A. ANDERSON, AND G. SCHUBERT 1986. Mantle circulation and the lateral migration of subducted slabs. *J. Geophys. Res.* **91,** 7205–7223.

GRIMM, R. E., AND R. J. PHILLIPS 1991. Gravity anomalies, compensation mechanisms, and the geodynamics of western Ishtar Terra, Venus. *J. Geophys. Res.* **96,** 8305–8324.

HANSEN, V. L., AND R. J. PHILLIPS 1993. Tectonics and volcanism of eastern Aphrodite Terra, Venus: No subduction, no spreading. *Science* **260,** 526–530.

HEAD, J. W., D. B. CAMPBELL, C. ELACHI, J. E. GUEST, D. P. MCKENZIE, R. S. SAUNDERS, G. G. SCHABER, AND G. SCHUBERT 1991. Venus volcanism: Initial Analysis from Magellan data. *Science* **252,** 276–288.

JANES, D. M., S. W. SQUYRES, D. L. BINDSCHANDLER, G. BAER, G. SCHUBERT, V. L. SHARPTON, AND E. L. STOFAN 1992. Geophysical models of the rift formation and evolution of coronae on Venus. *J. Geophys. Res.* **97,** 16055–16067.

JOHNSON, K., AND D. SANDWELL 1994. Lithospheric flexure on Venus. *Geophys. J. Int.*, in press.

KAULA, W. M. 1966. *Theory of Satellite Geodesy*. Blaisdell, Waltham, MA.

KONOPLIV, A. S., N. J. BORDERIES, P. W. CHODAS, E. J. CHRISTENSEN, W. L. SJOGREN, AND B. G. WILLIAMS 1993. Venus gravity and topography: 60th degree and order model. *Geophys. Res. Lett.* **20,** 2403–2406.

KONOPLIV, A. S., AND W. L. SJOGREN 1994. Venus spherical harmonic gravity model to degree and order 60. *Icarus.* **112,** 42–54.

MARKS, K. M., AND D. T. SANDWELL 1991. Analysis of geoid height versus topography for oceanic plateaus and swells using nonbiased linear regression. *J. Geophys. Res.* **96,** 8045–8055.

MCADOO, D. C. 1981. Geoid anomalies in the vicinity of subduction zones. *J. Geophys. Res.* **86,** 6073–6090.

MCKENZIE, D., P. G. FORD, C. JOHNSON, B. PARSONS, D. SANDWELL, S. SAUNDERS, AND S. C. SOLOMON 1992. Features on Venus generated by plate boundary processes. *J. Geophys. Res.* **97,** 13533–13544.

MOORE, W. B., AND G. SCHUBERT 1994. Lithospheric thickness and mantle/lithosphere density contrast beneath Beta Regio, Venus. *Geophys. Res. Lett.*, in press.

PARKER, R. L. 1973. The rapid calculation of potential anomalies. *Geophys. J. R. Astron. Soc.* **31,** 447–455.

PETTENGILL, G. H., P. G. FORD, AND R. J. WILT 1992. Venus surface radiothermal emission as observed by Magellan. *J. Geophys. Res.* **97,** 13091–13102.

PHILLIPS, R. J., R. E. GRIMM, AND M. C. MALL 1991. Hot-spot evolution and the global tectonics of Venus. *Science* **252,** 651–657.

RAPP, R. H., AND N. K. PAVLIS 1990. The development and analysis of geopotential coefficient models to spherical harmonic degree 360. *J. Geophys. Res.* **95,** 21885–21911.

SANDWELL, D. T., AND G. SCHUBERT 1992a. Flexural ridges, trenches, and outer rises around coronae on Venus. *J. Geophys. Res.* **97,** 16069–16083.

SANDWELL, D. T., AND G. SCHUBERT 1992b. Evidence for retrograde lithospheric subduction on Venus. *Science* **257,** 766–770.

SANDWELL, D. T., AND M. L. RENKIN 1988. Compensation of swells and plateaus in the North Pacific: No direct evidence for mantle convection. *J. Geophys. Res.* **93,** 2775–2783.

SCHUBERT, G., AND D. SANDWELL 1994. A global survey of possible subduction sites on Venus. *Icarus*, submitted.

SIMONS, M., B. H. HAGER, AND S. C. SOLOMON 1994. Global variations in the geoid/topography admittance of Venus. *Science* **264,** 798–803.

SMREKAR, S. E. 1994. Evidence for active hotspots on Venus from analysis of Magellan gravity data. Submitted for publication.

SMREKAR, S. E., AND R. J. PHILLIPS 1991. Venusian highlands: Geoid to topography ratios and their implications. *Earth Planetary Sci. Lett.* **107,** 582–597.

SOLOMON, S. C., J. W. HEAD, W. M. KAULA, D. MCKENZIE, B. PARSONS, R. J. PHILLIPS, G. SCHUBERT, AND M. TALWANI 1991. Venus tectonics: Initial analysis from Magellan. *Science* **252,** 297–313.

SQUYRES, S. W., D. M. JANES, G. BAER, D. L. BINDSCHADLER, G. SCHUBERT, V. L. SHARPTON, AND E. R. STOFAN 1992. The morphology and evolution of coronae on Venus. *J. Geophys. Res.* **97,** 13611–13634.

STOFAN, E. R., AND J. HEAD 1990. Coronae of Mnemosyne Regio: Morphology and origin. *Icarus* **83,** 216–243.

STOFAN, E. R., D. L. BINDSCHADLER, J. W. HEAD, AND E. M. PARMENTIER 1991. Coronae on Venus: Models of origin. *J. Geophys. Res.* **96,** 20933–20946.

STOFAN, E. R., V. L. SHARPTON, G. SCHUBERT, G. BEAR, D. L. BINDSCHADLER, D. M. JANES, AND S. W. SQUYRES 1992. Global distribution and characteristics of coronae and related features on Venus: Implications for origin and relation to mantle processes. *J. Geophys. Res.* **97,** 13347–13378.

TACKLEY, P. J., AND D. J. STEVENSON 1993. A mechanism for spontaneous self-perpetuating volcanism on the terrestrial planets. In *Flow and Creep in the Solar System: Observations, Modelling and Theory* (E. B. Stone and S. K. Runcorn, Eds.), pp. 307–321. Kluwer, Dordrecht, Netherlands.

TACKLEY, P. J., AND D. J. STEVENSON 1991. The production of small Venusian coronae by Rayleigh–Taylor instabilities in the uppermost mantle. *EOS Trans. AGU Supplement* **72** (44), 287. [Abstract]

TACKLEY, P. J., D. J. STEVENSON, AND D. R. SCOTT 1992. Volcanism by melt-driven Rayleigh-Taylor instability and possible consequences of melting for admittance ratios on Venus. In *Papers Presented to the*

International Colloquium on Venus, Lunar and Planetary Institute, Contribution 789, pp. 123–124. Houston, TX.

TURCOTTE, D. L. 1989. A heat pipe mechanism for volcanism and tectonics on Venus. *J. Geophys. Res.* **94,** 2779–2785.

TURCOTTE, D. L. 1993. An episodic hypothesis for Venusian tectonics. *J. Geophys. Res.* **98,** 17061–17068.

TURCOTTE, D. L., AND G. SCHUBERT 1982. *Geodynamics.* Wiley, New York.

TYLER, G. L., P. G. FORD, D. B. CAMPBELL, C. ELACHI, G. H. PETTENGILL, AND R. A. SIMPSON 1991. Magellan: Electrical and physical properties of Venus' surface. *Science* **252,** 265–269.

UYEDA, S., AND H. KANAMORI 1979. Back-arc opening and the mode of subduction. *J. Geophys. Res.* **84,** 1049–1061.